

The Wisconsin Plasma Astrophysics Laboratory

C. B. Forest^{1,†}, K. Flanagan¹, M. Brookhart¹, M. Clark¹, C. M. Cooper¹,
V. Désangles², J. Egedal¹, D. Endrizzi¹, I. V. Khalzov⁴, H. Li⁵, M. Miesch³,
J. Milhone¹, M. Nornberg¹, J. Olson¹, E. Peterson¹, F. Roesler¹,
A. Schekochihin^{6,7}, O. Schmitz¹, R. Siller¹, A. Spitkovsky⁸, A. Stemo¹,
J. Wallace¹, D. Weisberg¹ and E. Zweibel¹

¹Department of Physics, University of Wisconsin–Madison, Madison, WI 53706, USA

²Laboratoire de Physique de l’Ecole Normale Supérieure de Lyon, CNRS, and Université de Lyon,
46 Allée d’Italie, 69364 Lyon CEDEX 7, France

³High Altitude Observatory, National Center for Atmospheric Research, Boulder, CO 80307-3000, USA

⁴National Research Centre ‘Kurchatov Institute’, Moscow 123182, Russia

⁵Los Alamos National Laboratory, Los Alamos, NM 87545, USA

⁶Rudolph Peierls Centre for Theoretical Physics, University of Oxford, Oxford OX1 6NP, UK

⁷Merton College, Oxford OS1 4JD, UK

⁸Department of Astrophysical Sciences, Princeton University, Princeton, NJ 08540, USA

(Received 3 June 2015; revised 19 July 2015; accepted 22 July 2015)

The Wisconsin Plasma Astrophysics Laboratory (WiPAL) is a flexible user facility designed to study a range of astrophysically relevant plasma processes as well as novel geometries that mimic astrophysical systems. A multi-cusp magnetic bucket constructed from strong samarium cobalt permanent magnets now confines a 10 m^3 , fully ionized, magnetic-field-free plasma in a spherical geometry. Plasma parameters of $T_e \approx 5$ to 20 eV and $n_e \approx 10^{11}$ to $5 \times 10^{12}\text{ cm}^{-3}$ provide an ideal testbed for a range of astrophysical experiments, including self-exciting dynamos, collisionless magnetic reconnection, jet stability, stellar winds and more. This article describes the capabilities of WiPAL, along with several experiments, in both operating and planning stages, that illustrate the range of possibilities for future users.

1. Introduction

During the past five years, a medium-scale multi-investigator experimental plasma facility – the Wisconsin Plasma Astrophysics Laboratory (WiPAL) – has been constructed and is now in operation at the University of Wisconsin–Madison. At the heart of the facility is a high bay that houses a 3 m diameter spherical multi-cusp confinement device (see figure 1). Its flexibility and diagnostic access allow WiPAL to currently support two major experiments: the Madison Plasma Dynamo Experiment (MPDX) and the Terrestrial Reconnection Experiment (TREX), along with several new experiments being added in the near future. Both the flexible design of the

† Email address for correspondence: cbforest@wisc.edu

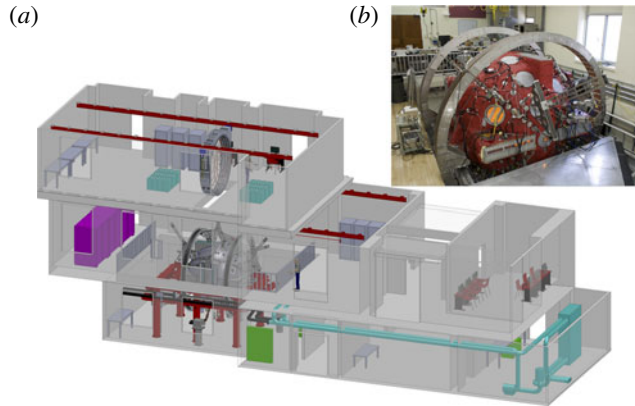


FIGURE 1. (a) The WiPAL facility consists of a main laboratory space where the vessel is housed and several auxiliary spaces for high-voltage power management, water pumping, computer control and housing the TREX insert. (b) The 3 m diameter vessel covered with arrays of probes and clear viewing ports.

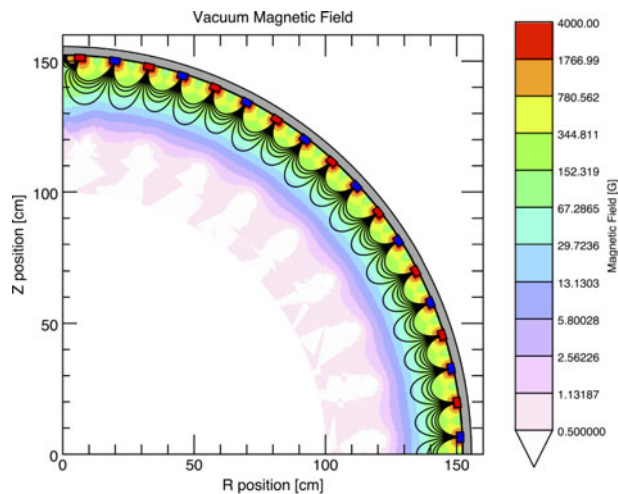


FIGURE 2. A static calculation of the vacuum magnetic field from the permanent magnets at the edge and the background earth field. This calculation has been normalized by Hall probe measurements along a radial chord.

facility and the shared hardware between experiments allow for a rapid turn-around between different configurations.

The purpose of this paper is to describe the physical parameter regimes that can be achieved in WiPAL, to illustrate its flexibility, and to show how the plasma confinement scheme lends itself to many experiments of interest to the astrophysics and fundamental plasma physics communities. Already, this facility has transitioned from a single-purpose experiment focused on plasma dynamos (MPDX) to a multi-investigator facility accommodating a new reconnection experiment (TREX). In the future, WiPAL will transition into a collaborative user facility open to other laboratory astrophysics research groups. This paper illustrates the potential

of the facility by describing (in addition to MPDX and TREX) several additional experiments that are now being pursued: acoustic and Alfvén wave propagation in connection with helioseismology; pulsar and stellar wind launching from a rotating dipolar magnetosphere; jet formation and propagation into background plasma; and small-scale high-power helicity injection. In addition to these experimental efforts, numerical and theoretical computations, often carried out with identical dimensionless parameters, are used to create predictive models and inform elements of design.

This article begins with an overview of WiPAL, along with experimentally achieved plasma parameters. Then a description is given of the diagnostic suite and of the magnetic cusp confinement used in WiPAL. This is followed by brief summaries of experiments that are under way or in development.

2. Description of the facility

The WiPAL facility (shown in figure 1) consists of the plasma confinement vessel and the associated infrastructure (high bay, electrical power, water cooling and associated laboratories). The vacuum vessel consists of two 1.5 m radius cast-aluminium hemispheres mounted on a track that can be separated during a vacuum opening. This provides the opportunity for quickly inserting different devices inside the WiPAL vessel. For example, a transition from full MPDX operation to the TREX configuration requires only a few days.

Nearly 3000 samarium cobalt (SmCo) permanent magnets (each with $|\mathbf{B}| > 3$ kG at their surface) are held in axisymmetric rings on the inside of the vessel. These rings alternate in polarity to form a strong high-order multipole field that decreases in strength to the background earth field within 20 cm of the vessel wall (shown in figure 2). This edge-localized cusp field provides sufficient plasma confinement to achieve the parameters listed in table 1 while leaving the ions in the core unmagnetized. The rings were carefully produced to assure axisymmetry, thus reducing many aspects of WiPAL experiments to two dimensions. Since all the magnetic field variation is in the radial and polar directions, gradient and curvature drifts are azimuthal. This leads to an azimuthal symmetry of the generated plasmas, thereby reducing convective losses associated with magnetic ripple.

To date, argon and helium plasmas have been created and heated by an array of hot emissive lanthanum hexaboride (LaB_6) cathodes, each independently powered by separate 30 kW power supplies (currently 12, with 18 planned). See figure 3 for an example discharge in a typical helium plasma. Five 20 kW magnetrons at 2.45 GHz are in the process of being added to independently heat electrons through electron cyclotron resonance (ECR) heating in the magnetized edge, bringing the maximum steady-state input power to ~ 650 kW. These sources are quasi-stationary, meaning that plasmas can be sustained for tens of seconds limited only by vessel heating.

A unique capability of the facility is the ability to control the plasma rotation at the boundary (Cooper *et al.* 2014). Early experiments at the facility have been focused on studying highly conducting, flow-dominated plasmas and understanding the interface between magnetized and unmagnetized plasma conditions. Plasmas have been stirred at speeds up to 10 km s^{-1} in the azimuthal direction by applying a $\mathbf{J} \times \mathbf{B}$ torque in the magnetized edge region. Each of the cathodes are mounted on a motorized stage so their insertion depth can be quickly and accurately set between shots. Cathodes pushed into the unmagnetized bulk of the plasma ionize and heat the plasma, while cathodes pulled back into the magnetized region draw current across magnetic field lines, injecting torque into the plasma. This torque is viscously

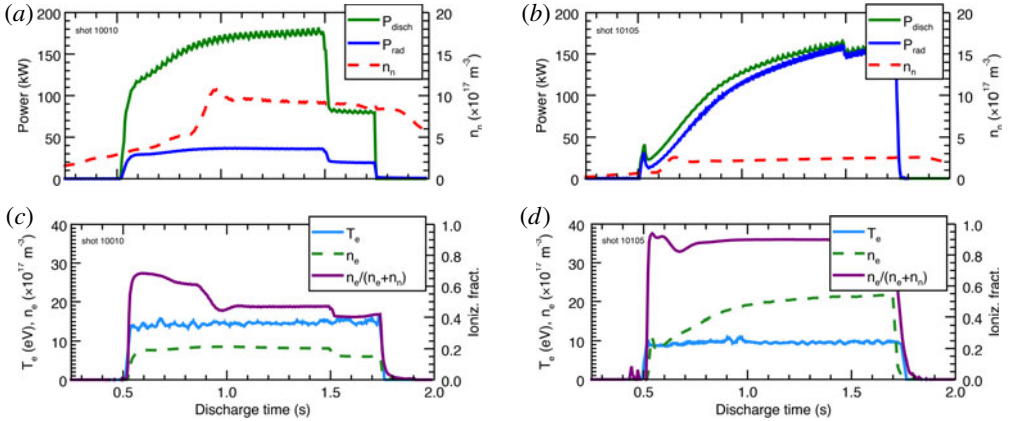


FIGURE 3. Time traces of plasma parameters and input power from a typical WiPAL discharge in helium (*a,c*) and argon (*b,d*). Radiated power is measured with a bolometer, n_n is measured with a pressure gauge at the edge of the vessel (assuming room-temperature neutrals), T_e is measured with a Langmuir probe inserted into the unmagnetized bulk, and n_e is measured with the millimetre-wave interferometer system.

Parameter	Achieved	Achieved	Projected
Gas	He	Ar	He
P_{in} (kW)	300	300	650
T_e (eV)	20	10	40
T_i (eV)	1.5	3	10
n_e (10^{12} cm $^{-3}$)	2.5	4	10
$f_{\%}$ (%)	75	90	99
V (km s $^{-1}$)	10	5	20
$Rm = VL/\eta$	900	350	5000
$Re = VL/\nu$	600	1300	1000
B_{equip} (G)	14	29	60
β at 10 g	8	8	20

TABLE 1. Table of parameters achieved to date in separate discharges (with 10 of 18 possible cathodes and no ECR heating) as well as projected parameters. The ionization fraction, $f_{\%}$, is calculated using neutral pressure at the vessel wall and line-integrated electron density.

coupled to the unmagnetized core. This boundary-driven flow scheme was designed for dynamo studies on MPDX, but will be used to study other features of fast-moving plasmas in the WiPAL facility.

Additionally, several capacitor banks with ignitron switching have been used to drive short pulse reconnection experiments in TREX (§ 3.3) and to inject current for plasma jet experiments (§ 3.6). For example, initial reconnection experiments utilized an up to 10 kV, 100 μ F capacitor bank to drive approximately 20 kA for 250 μ s, generating a 10 G reconnection field from a two-turn internal coil. WiPAL is also equipped with a large Helmholtz coil pair which provides a uniform field throughout the plasma volume of up to 275 G.

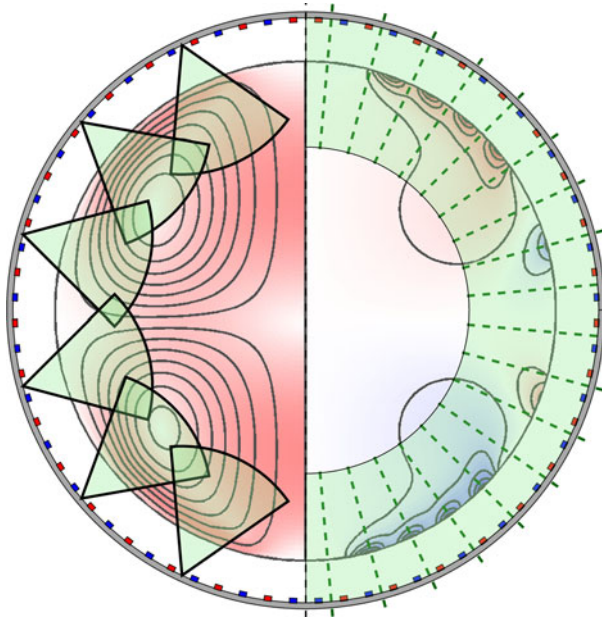


FIGURE 4. An example of a predicted dynamo-capable axisymmetric flow, with poloidal flow (left) and toroidal flow (right) is well diagnosed by the full motorized probe suite. WiPAL probe coverage will include both sweep probes (six total, left) and linear probes (18 total, right).

2.1. Major diagnostics

The WiPAL vessel is covered with approximately 200 ports for diagnostic access of plasma discharges via robotic probe arrays and advanced optical measurements. Owing to the high temperature and steady-state nature of WiPAL discharges, *in situ* probes have been carefully designed to accommodate high heat flux. Additionally, the small loss area provided by the cusp confinement is increased significantly by inserting probes into the plasma. Motivated by these issues, a suite of non-invasive optical diagnostics has been developed and works in concert with inserted probes.

2.1.1. Two-dimensional probe systems

Most plasma astrophysics experiments require high-resolution, two-dimensional (2D) measurements obtained using internal probe arrays. To meet this need, WiPAL has several robotically controlled probe drive systems in place. Two types of scanning systems are used, as shown in figure 4. The first probe system is a set of sweeping probes (one currently installed, with six planned) that are inserted through a single ball-joint vacuum seal port, combining radial and angular motion to sweep out a 2D plane. Two stepper-motor-controlled transverse stages allow the regions shown to be scanned shot-to-shot with arbitrary resolution. The second probe system is an array of single-axis probes that are inserted every 10° in latitude. These probes have a single stepper-motor drive, allowing radial shot-to-shot scans.

The main probe type to be used in WiPAL is a combination velocity–magnetic probe. Each probe tip consists of two Mach probes (four planar Langmuir faces collecting ion saturation current) to measure two orthogonal components of \mathbf{v} . Development is under way to add three Hall sensors to measure the entire

three-dimensional (3D) \mathbf{B} field in each probe tip. These probes are designed to withstand long, warm plasma pulses, utilizing a thermally conductive copper shaft paired with an electrically and thermally insulating quartz shield. The lifetime of probes is ultimately limited by accumulated heat load over many plasma pulses, but thermocouple temperature monitoring facilitates optimization of plasma duty cycle versus probe temperature.

Increased probe coverage also leads to diminished plasma performance because plasma losses to the exposed probe area can be much larger than the edge losses through the permanent magnet cusp field. Motorized probes allow for flexibility in controlling the plasma loss area. For example, staggered radial scans of various probes can keep the loss area constant while still mapping out the full extent of probe coverage.

The 2D structure of the magnetic field on the surface of the plasma will be measured using an array of 64 external magnetic probes placed in the region between the plasma and the vessel wall. These probes will consist of three-axis Hall probes for measuring low-frequency magnetic fields as well as two orthogonal Mirnov coils for measuring higher-frequency fluctuations. The final implementation of this full array will resolve $\ell = 8$ harmonics in the polar direction and $m = 8$ harmonics in the toroidal direction.

In addition to this collection of internal probes, WiPAL is equipped with an array of optical diagnostics. A millimetre-wave interferometer system measures the line-integrated electron density; a Fabry–Perot spectrometer provides measurements of ion temperature; and optical emission spectroscopy (OES) can be used to determine neutral and ion density profiles, electron temperature and electron density. All of these systems provide precise, non-invasive measurements of key plasma parameters without increasing the plasma loss area.

2.1.2. Absolute density measurements

WiPAL is equipped with a heterodyne millimetre-wave (320 GHz) interferometer system designed to measure chord-integrated absolute electron density via wave phase shifts. This system is very similar to interferometers used on the helically symmetric experiment (HSX) and the Madison symmetric torus (MST) (Deng *et al.* 2003, 2006). Time resolution of density measurements is set by the intermediate frequency (IF) of the variable-frequency source. Typically, the IF is set to $f \sim 1$ MHz, but is adjustable from 0.1 to 100 MHz.

At WiPAL densities of $n_e = 10^{11}$ to 5×10^{12} cm⁻³, phase shifts of several fringes (one fringe corresponds to a 2π phase shift between the reference and plasma beams) must be measured. Additionally, owing to time resolution requirements, this measurement must be made at frequencies up to several megahertz. This constraint is met by using a high-speed field-programmable gate array (FPGA) programmed to compute the phase at each period of the reference beam. The ultimate density resolution is set by the speed of the FPGA clock relative to the IF frequency and yields $\delta n \sim 10^{10}$ cm⁻³ for an IF of 1 MHz.

This absolute electron density measurement is used to calibrate Langmuir probe data for point measurements as well as to constrain neutral emission models for spectroscopic measurements of the electron temperature (§ 2.1.4). Because of the good time and density resolution, this diagnostic will be used in TREX to measure density fluctuations associated with magnetic reconnection.

2.1.3. Ion temperature and flow

Doppler-shifted line emission is measured using a Fabry–Perot spectrometer. Plasma light is passively collected from either the $\lambda = 488$ nm argon ion line or the $\lambda = 468.6$ nm helium ion line complex depending on the working gas. By imaging these ion lines at a high resolution, the Fabry–Perot captures the line-integrated ion velocity distribution function. Ion temperature is inferred from the thermal broadening of the lines, while velocity can be measured via the Doppler shift of the peak away from its stationary value.

The Fabry–Perot system has several distinct advantages over a grating-type spectrometer. For a comparable sized grating, the Fabry–Perot has an increase of nearly 100 times the resolving power. Additionally, because the output of the Fabry–Perot is a symmetric ring structure where $r^2 \propto \lambda$, integration around the rings can greatly increase signal-to-noise ratio. This procedure, called ring summing, results in a sensitivity gain of 10–30 compared to linear cuts of the pattern (Coakley *et al.* 1996). Additionally, it allows for relatively short integration times (roughly 1 s in this system) using a standard digital camera. WiPAL also has a high-performance intensified charge-coupled device (CCD) camera capable of taking even shorter exposures (approximately 0.1 s) for multiple measurements during discharges. The typical resolution (i.e. error bars) of Fabry–Perot ion temperature measurements is $\delta T_i \approx 0.05$ eV and the velocity resolution is of the order $\delta v \approx 10$ m s⁻¹.

2.1.4. Electron temperature and distribution

Several survey spectrometers are used to measure emission throughout the visible spectrum with lower spectral resolution than the Fabry–Perot. The spectrometers capture segments of the near-ultraviolet to the near-infrared range, either monitoring the entire spectrum at low resolution (300–888 nm at 0.387 nm) or small segments at a higher resolution (381–511 nm at 0.045 nm). Spectra are continuously captured through WiPAL discharges with exposure times of 2–80 ms and rates of 10–50 Hz, which provide a time history relevant for long-pulse time scales.

The OES system, calibrated by the millimetre-wave absolute density measurement, can estimate the electron temperature and ionization fraction. Line ratios are compared to collisional radiative models calibrated to data from other experiments and used to infer T_e while including additional corrections due to non-Maxwellian electron distribution functions in argon plasmas (Boffard *et al.* 2010; Wang *et al.* 2013). In helium, line ratios can also be used to determine T_e and n_e with similar modelling (Schmitz *et al.* 2008). Good agreement has been found between the models and the data in the regimes calibrated for tokamak scrape-off layers (high T_e , n_e). Work is under way to benchmark these models for more relevant parameters. In addition to using the OES system for its own measurements, WiPAL offers an opportunity to extend these calibrations to regimes relevant for laboratory plasma astrophysics.

3. Major experiments in WiPAL

3.1. Large multi-cusp plasma confinement

WiPAL is the largest axisymmetric magnetic ring cusp ever constructed for confining plasmas. The permanent magnets effectively limit the loss area to ~ 1 % of the total vacuum vessel surface area, which in turn leads to high, steady-state confinement. The combination of WiPAL's cusp confinement and diagnostic capabilities presents an opportunity for studying and characterizing the confinement of magnetic cusps. The cusp field is created by 36 rings of alternating-polarity magnets, as shown in figure 2.

This field is localized to the edge, dropping off to the background earth field within 20 cm of the vessel wall. Plasma losses in this configuration are limited to a small cusp width on the face of each magnet. To electrically isolate the plasma from the vessel wall, each magnet is covered by a thin insulating ceramic tile.

The long established empirical loss width for a magnetic cusp is the hybrid gyroradius $w \sim \sqrt{\rho_i \rho_e}$ (Hershkowitz, Leung & Romesser 1975), yet newer studies have found a scaling with neutral pressure which suggests more detailed physics than was previously employed (Hubble *et al.* 2014). Since WiPAL is able to create and sustain plasmas at very low pressures, this neutral pressure scaling can be investigated over several orders of magnitude. Accurate measurements of the ion velocity distribution at the cusp can be made with the Fabry–Perot system. Additionally, owing to the insulating boundary condition, *in situ* probes at the ceramic tile can directly measure the loss width. Understanding the loss width scalings in a magnetic cusp is important not only for predicting plasma confinement in WiPAL but also to a number of other applications such as plasma processing (Malik *et al.* 1994), Hall thrusters (Sengupta 2009) and neutral beam injectors (Stirling *et al.* 1979).

3.2. Self-exciting dynamos

Astrophysical plasmas are often characterized by high magnetic Reynolds numbers ($Rm = VL/\eta$, where η is the magnetic diffusivity, V is a characteristic flow speed and L is the system size) wherein turbulent, flow-dominated plasmas continuously transform kinetic flow energy into magnetic energy. Understanding this energy transformation and predicting what form the magnetic field might take, be it small-scale turbulent magnetic fields or large-scale magnetic flux, is the dynamo problem. The theory of dynamos has shown that the scales at which the magnetic energy grows are largely determined by the relative values of the magnetic Reynolds number and the fluid Reynolds number ($Re = VL/\nu$, where ν is the dynamic viscosity). The ratio $Pm = Rm/Re$, called the magnetic Prandtl number, is thought to be a critical parameter that governs the nature of many astrophysical phenomena, since it sets the relative collisional dissipation scales of the fields and flows. Astrophysical plasmas span a wide range of Pm ; diffuse plasmas have $Pm \gg 1$ whereas denser plasmas have $Pm \ll 1$.

Dynamos can be classified as small-scale or large-scale. Small-scale dynamos tend to generate magnetic energy but little net magnetic flux, whereas large-scale dynamos generate both net flux and energy. While the process by which turbulence generates magnetic energy at small scales seems theoretically well understood (Schekochihin *et al.* 2004; Iskakov *et al.* 2007), understanding how a large-scale magnetic field self-organizes from small-scale magnetic fluctuations in astrophysical systems remains a grand challenge for plasma astrophysics.

Studying plasma dynamos in the laboratory requires a previously unexplored regime of laboratory plasmas. Unmagnetized, fast-flowing and highly conducting plasmas are required so that magnetic fields can be stretched and amplified by the plasma inertia. Cast in dimensionless terms, dynamo action requires plasmas with high Rm and high Alfvén Mach number ($Ma = V/V_A \gg 1$). The particular geometries being pursued in the MPDX configuration of WiPAL build upon similar geometries used by liquid-metal experiments. Mechanically stirred liquid-sodium experiments have observed spontaneous magnetic field generation (Monchaux *et al.* 2007, 2009; Gallet *et al.* 2012) and have added to our understanding of astrophysical and geophysical dynamos (Lathrop & Forest 2011). A plasma experiment has the potential to extend these studies to parameters more relevant to astrophysics. Beyond the obvious fact

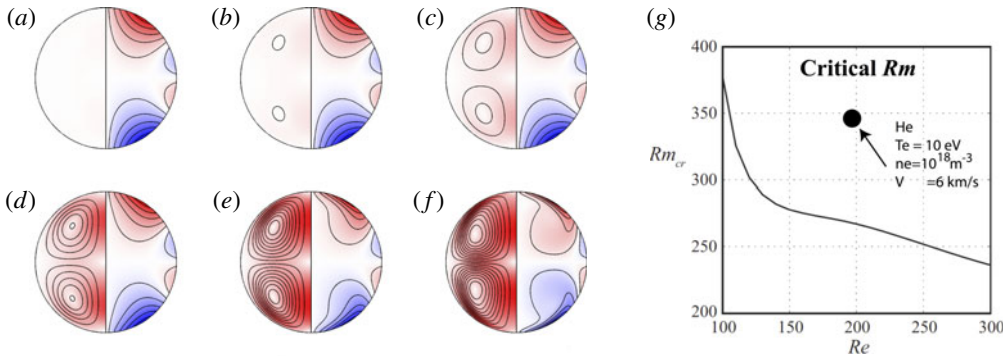


FIGURE 5. (a–f) Hydrodynamic simulations of edge-driven, two-vortex axisymmetric flow in He for increasing Re : (a) 1, (b) 3, (c) 10, (d) 30, (e) 100 and (f) 300. Axis of rotation and symmetry are vertical; left hemispheres show poloidal flow streamlines and poloidal flow magnitude; right hemispheres show toroidal flow contours. The poloidal flow scale is amplified $4\times$ relative to the toroidal flow scale. (g) Kinematic dynamo growth rate of the flows shown in (a–f). Increasing Re results in a larger amount of kinetic energy in poloidal flows, which in turn lowers the critical Rm required for positive magnetic eigenmode growth. Flow is only axisymmetric for $Re < 300$; hydrodynamic instabilities produce non-axisymmetric modes at higher Re , requiring full 3D solutions to the induction equation.

that most naturally occurring dynamos are plasmas, the use of plasma rather than liquid metals corresponds to magnetic Reynolds numbers increased by a factor of 10 or larger. Additionally, viscosity can be varied independently of the conductivity, with Pm ranging from 0.1 to 10, reflecting the wide range found in different astrophysical systems.

Extensive modelling and theoretical work have been carried out to find flow schemes for MPDX that excite a large-scale dynamo (Spence, Reuter & Forest 2009; Katz *et al.* 2012; Khalzov *et al.* 2012*a,b*; Khalzov, Cooper & Forest 2013). By biasing the cathodes in the magnetized edge, torque is injected at the boundary of the plasma and is viscously coupled to the core. Dynamo-relevant flows are found by solving the Navier–Stokes equation for a particular boundary condition imposed by the cathode drive. The resulting flow is then used to solve the kinematic dynamo equation. One such flow that results in dynamo action is shown in figure 5. The imposed boundary condition drives two counter-rotating vortices in each hemisphere with a small flow direction reversal near the equator. For fairly modest Rm and Re , positive dynamo growth is expected. Work on MPDX is currently directed at optimizing the flow drive and attempting to create this two-vortex flow.

Fast small-scale dynamos can be excited by chaotic flows with the high values of Rm and Pm possible in WiPAL. Chaotic flows with positive Lyapunov exponents could be achieved with large Re turbulence or by using time-dependent and highly viscous laminar flows (Khalzov *et al.* 2013). Three-dimensional numerical simulations using turbulent flows where $Re \sim 500$ and Rm is very high have confirmed that turbulent, small-scale magnetic fields naturally develop in high- Pm plasmas. Moreover, the magnetic amplification of these flows is roughly independent of Rm as Rm continues to increase, a hallmark of fast dynamos. Figure 6 shows several example of flows where fast dynamo growth is possible. Simulations predict fast dynamo growth at plasma parameters that can be achieved with increased input power from ECR heating.

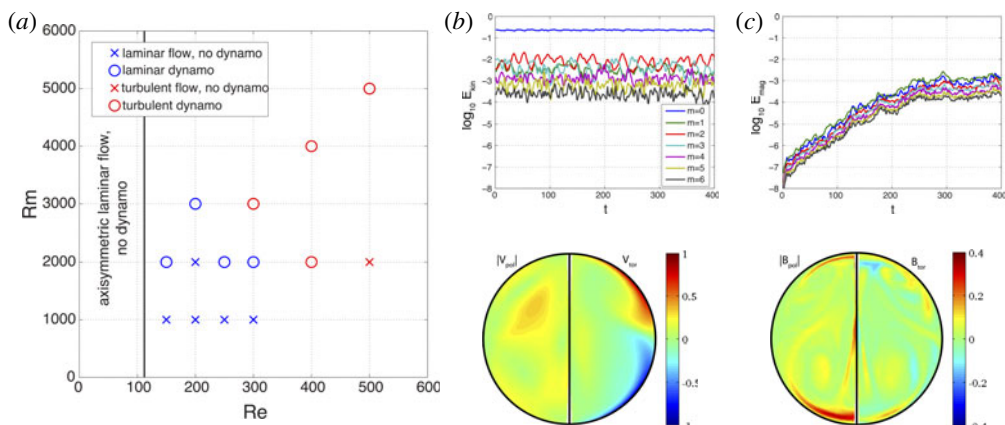


FIGURE 6. Numerical solutions for turbulence-driven small-scale dynamo and evidence for large-scale field generation. To achieve $Rm = 2000$ and $Re = 400$ corresponds to a helium plasma with $V_{max} = 10 \text{ km s}^{-1}$, $T_e = 30 \text{ eV}$, $T_i = 1.2 \text{ eV}$, $n_e = 10^{18} \text{ m}^{-3}$ and $Z_{eff} = 1.2$. Panel (a) shows where simulations find turbulent dynamos in Re and Rm space.

Because Rm is very large in most astrophysical systems, virtually any astrophysical dynamo must be fast. Understanding the conditions for fast dynamos and exploring whether they can generate magnetic fields on large scales is an open problem in plasma astrophysics.

3.3. Magnetic reconnection

One of the fundamental processes in nearly all magnetized plasmas is magnetic reconnection: a change in the magnetic topology of the plasma that converts stored magnetic energy into particle kinetic energy (Priest & Forbes 2000). Given its importance, magnetic reconnection has been studied extensively through theory, numerical computation, spacecraft observations and laboratory experiments. In recent years, new frontiers have emerged with an emphasis on particle energization, reconnection with multiple X-lines in large systems, the role of kinetic effects in collisionless reconnection, and extending the evolution of reconnection from two dimensions to three. For experiments to remain relevant and to advance this maturing field, new devices are needed that access these regimes. To address this need, we are now operating the Terrestrial Reconnection Experiment (TREX), which is the largest dedicated reconnection experiment to date. In addition to WiPAL's existing vacuum vessel, plasma confinement, heating and diagnostic suite, TREX consists of a cylindrical insert holding coils used for driving reconnection (shown in figure 7). The parameter regimes expected for TREX are shown in table 2. The full operation of TREX within WiPAL renders the facility unique in its ability to address the expanding frontiers of reconnection research.

An important component to the implementation of TREX into the WiPAL user facility is the cylindrical insert housing the reconnection drive coils and the addition of a toroidal field coil. The insert and TF coil allow TREX to access multiple magnetic configurations (e.g. antiparallel reconnection, strong guide-field reconnection and 3D reconnection), as well as a wider range of reconnection regimes. TREX also utilizes a suite of probe arrays specially developed to characterize reconnection

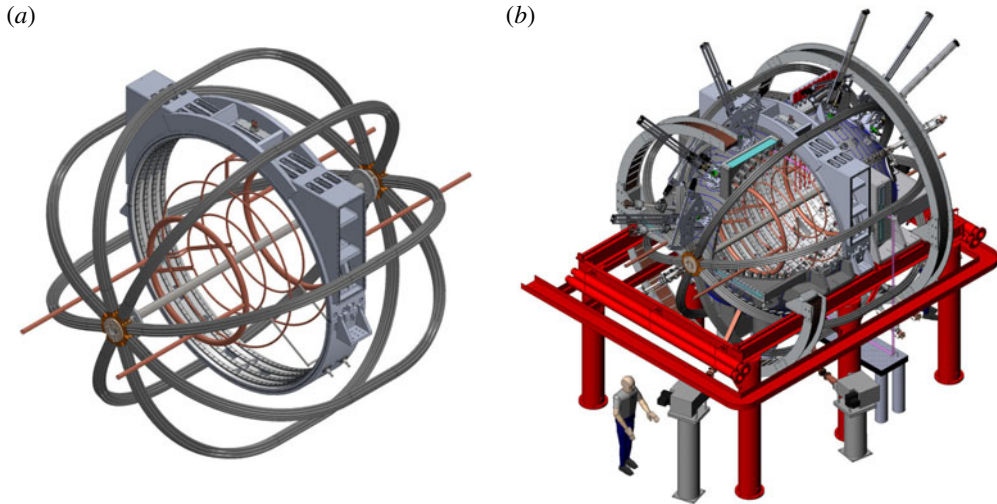


FIGURE 7. (a) Toroidal field coils and a cylindrical insert holding additional coils for driving reconnection will be inserted into the WiPAL vessel. (b) The large set of external Helmholtz coils is a recent upgrade to the WiPAL facility with utility for many future experiments.

	n_e (10^{18} m^{-3})	T_e (eV)	B_r (T)	B_g (T)	L (m)
Terrestrial Reconnection Experiment (TREX; U. Wisconsin–Madison)	0.1–10	8–40	0.04	0–0.3	0.8–1.8
Magnetic Reconnection Experiment (MRX; Princeton U.)	2–100	5–10	0.03	0–0.1	0.3–0.8
Versatile Toroidal Facility (VTF; MIT)	0.1–1	8–30	0.01	0.1	0.3

TABLE 2. Key parameters for various reconnection experiments in hydrogen plasmas, where B_r and B_g are the reconnecting and guide fields, respectively.

dynamics. These include stationary magnetic and electric probes along with sweep probe arrays that allow for a 2D region to be mapped out over repeated shots (§ 2.1.1). The necessary dynamics can be captured on time scales up to 20 MHz with the diagnostic suite. For a desired value of the reconnecting field, the configuration must be driven at the corresponding loop voltage $V_{loop} = 2\pi R(0.1v_A B_r)$. For example, a loop voltage of 5 kV for a 150 G reconnecting field is required to access fast reconnection in a hydrogen plasma. This consideration has necessitated the development of reliable, high-power pulsing circuits utilizing class D ignitron switches to drive reconnection. These drive circuits can be pulsed as fast as every 10 s.

So far, the term ‘collisionless reconnection’ has referred to systems where the electron and ion distributions can remain near Maxwellian, but the collisionality is sufficiently low that their collective fluid behaviours decouple at the ion scale and Hall currents become important. However, in a truly collisionless plasma, pressure anisotropy develops, which strongly impacts the properties of the reconnection process in ways not accounted for in traditional Hall reconnection. In fact, spacecraft observations (Hwang *et al.* 2013) and kinetic simulations at the full ion-to-electron

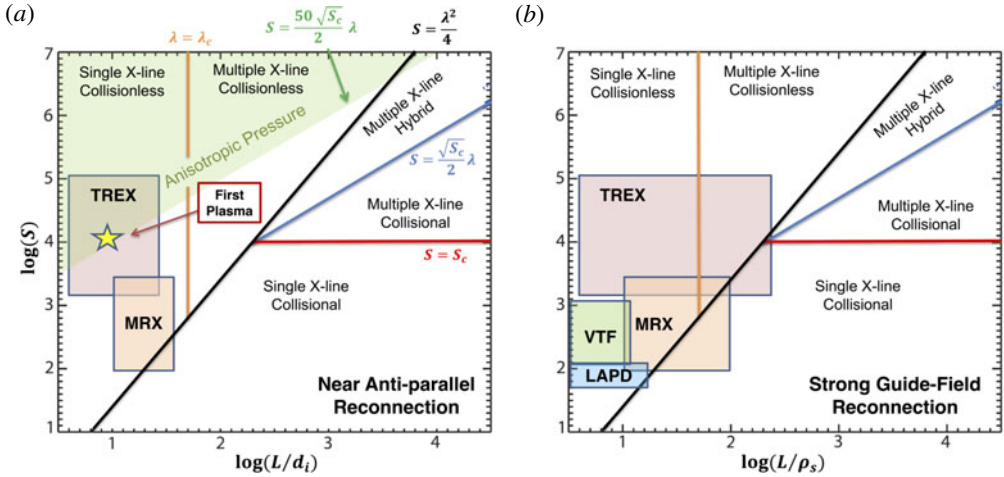


FIGURE 8. Reconnection phase-space diagrams for weak guide-field reconnection (a) and strong guide-field reconnection (b) identifying various regimes of reconnection. The star characterizes the first plasma obtained with TREX, demonstrating its ability to access the new collisionless reconnection regime.

mass ratio (Le *et al.* 2015) show that large-scale current layers are driven by electron pressure anisotropy that builds in the reconnection region due to kinetic electron trapping effects. To maintain pressure anisotropy, the time between electron collisions must be long compared with the full transit time of a fluid element through the reconnection layer (Egedal, Le & Daughton 2013; Le *et al.* 2015).

As a valuable tool for displaying the various regimes of reconnection and their transitions, Daughton & Roytershteyn (2012) developed the reconnection phase diagram spanned by the Lundquist number S and the normalized system size λ with respect to the ion sound Larmor radius, $\rho_s = \sqrt{m_i(T_e + T_i)}/eB$, or the ion skin depth, $d_i = c/\omega_{pi}$, for strong and weak guide-field reconnection, respectively (Ji & Daughton 2011). A convenient way of representing the constraint for anisotropic pressure on a system is the condition $S > 10(m_i/m_e)(L/d_i)$. The anisotropic pressure region of this phase space is shown in figure 8. As indicated by the star, TREX has already demonstrated its ability to access this regime of collisionless reconnection. TREX is able to experimentally study the role that electron pressure anisotropy has on particle heating. In addition, the narrow current layers driven by the anisotropy may in 3D be unstable to reconnection at oblique angles. This effect of 3D reconnection may be important to the self-consistent evolution and generation of reconnection with multiple X-lines.

3.4. Acoustic waves, helioseismology and angular momentum transport

The WiPAL facility can study both basic solar plasma phenomena as well as longstanding mysteries explored by the heliophysics community, such as angular momentum transport in the Sun and other late-type stars. It is well established from observations and modelling that late-type stars with convective envelopes spin down as they age due to torques exerted by magnetized stellar winds (Mestel 1968; Barnes 2007; Matt *et al.* 2015). It is less well understood how this angular momentum loss is transmitted through their convection zones and into their radiative cores. Helioseismic probing of our own Sun suggests that this coupling is efficient in the sense that

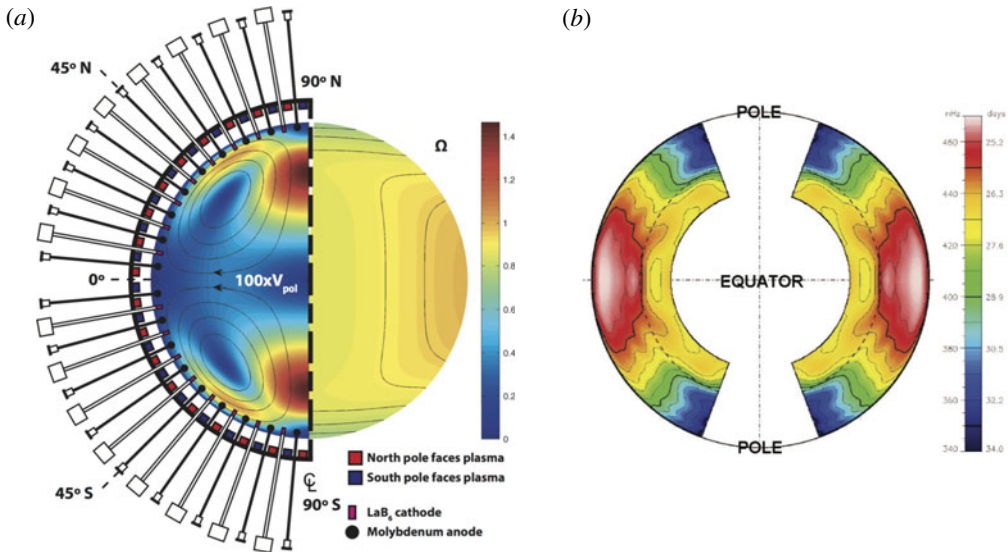


FIGURE 9. (a) A simulation of solar-like flow inside the WiPAL vessel with streamlines of poloidal flow. The internal rotation profile of the Sun is inferred from helioseismic inversions (Thompson 2014). Pink/red denote fast rotation and blue/green denote slower rotation as indicated by the colour bar. Inversions near the rotation axis are unreliable and are thus omitted from the plot. (b) The image of the angular velocity profile is reflected about the rotation axis in order to illustrate the full spherical geometry.

the radiative core currently has a rotation rate that is comparable to the convective envelope (Thompson *et al.* 2003). However, these same helioseismic inversions reveal that the radiative core is rotating nearly uniformly while the convection zone rotates differentially, with a $\sim 30\%$ decrease in angular velocity from equator to pole (Thompson *et al.* 2003). The transition between these two distinct rotation regimes is called the solar tachocline, which overlaps with the base of the convection zone and the convective overshoot region.

Angular momentum transport within the solar convection zone is attributed to turbulent magnetized convection and occurs on convective time scales of weeks to months. By contrast, the transport of angular momentum across the solar tachocline, coupling the core and envelope, is thought to occur on much longer time scales of millions to billions of years (Spiegel & Zahn 1992). Our current understanding of both short-term and long-term angular momentum transport in the Sun relies on incomplete and indirect observational data (e.g. helioseismic inversions) and numerical magnetohydrodynamic (MHD) models. WiPAL offers an opportunity to study some aspects of the relevant dynamics in the laboratory for the first time.

Using the drive system as MPDX, a solar-like flow can be programmed at the boundary of the WiPAL vessel. A calculation of the structure of this flow is shown on figure 9(a). This flow is aimed at mimicking the helioseismic inversion, shown on figure 9(b), with strong toroidal rotation near the equator. Careful scrutiny of how such a boundary-forced differential rotation spreads into the interior through meridional flows, viscous diffusion, thermal gradients and magnetic tension will provide insight into core–envelope coupling and the resulting spin-down of late-type stars. Magnetic tension in particular is thought to be responsible for maintaining the uniform rotation

of the radiative interior by suppressing shear, as described by Ferraro's theorem (MacGregor & Charbonneau 1999). Furthermore, inserting a dipole electromagnet into the core of the WiPAL vessel will create a mock tachocline, testing the structure and stability of the boundary layer proposed by magnetic tachocline confinement models (e.g., Gough & McIntyre 1998).

By exciting the acoustic normal mode spectrum of a spherical plasma with external antennas, the stationary plasma response can be characterized. It is predicted by theory and observed in the Sun that these normal modes split when rotation is introduced (Christensen-Dalsgaard 2002). Helioseismology relies on these mode splittings at different locations on the Sun to discern the flow profiles of the interior. A similar analysis is available at WiPAL with the addition of the external magnetic probe array described in § 2.1.1. When differential rotation is imposed at the boundary, the resulting spectra can be spatially decomposed and compared to the stationary mode structure. A mathematical inversion can then be used to propose likely candidates for internal global flow profiles, which can be benchmarked by Mach probe measurements under similar conditions. This would form the basis of a minimally invasive, global flow profile diagnostic at WiPAL akin to helioseismic inversions.

Using this helioseismic diagnostic and solar flow drive, WiPAL will study the short-term angular momentum transport in the solar convection zone. Experimental set-ups, such as that shown in figure 9, can be used to investigate the physics of turbulent transport. In the Sun, turbulent angular momentum transport is thought to be responsible not only for sustaining the solar differential rotation, but also for regulating the amplitude and structure of the meridional flow by means of gyroscopic pumping (Miesch & Hindman 2011). More generally, turbulent angular momentum transport, mean flows and thermal gradients in the solar convection zone are all thought to be intimately linked through nonlinear feedbacks that can be explored with WiPAL.

3.5. Centrifugally driven stellar winds

Plasma wind launched from star surfaces carries stellar magnetic field into the local heliosphere and out to the interstellar medium. This system is complex and is governed by a range of processes, including magnetic reconnection, turbulence and particle heating, all topics of present-day heliospheric research. One aspect that has received little experimental attention is the magnetic topology of the advected magnetic field in the interface region between the magnetically dominated corona and the flow-dominated wind. This region is critical both in creating the Parker spiral and in determining the mass loss rates of stars. The centrifugal wind experiment (CWE) at WiPAL will explore centrifugal breakout of wind from spinning dipolar magnetospheres.

The winds of rapidly rotating giant stars and pulsars are particularly relevant. For rapidly rotating giant stars, centrifugal breakout has been predicted to proceed in episodic bursts of plasmoids (ud Doula, Townsend & Owocki 2006). Recent observations by the Microvariability and Oscillations of STars (MOST) telescope have called into question the validity of this breakout model, suggesting instead a smooth outflow (Townsend *et al.* 2013). Modelling centrifugal breakout in a laboratory setting can advance our understanding of this phenomenon. Pulsars have been extensively modelled using analytical MHD and 3D particle-in-cell (PIC) simulations of both aligned and obliquely rotating magnetospheres (Spitkovsky 2006; Philippov & Spitkovsky 2014). Both cases predict the creation of a magnetic Y-point where the

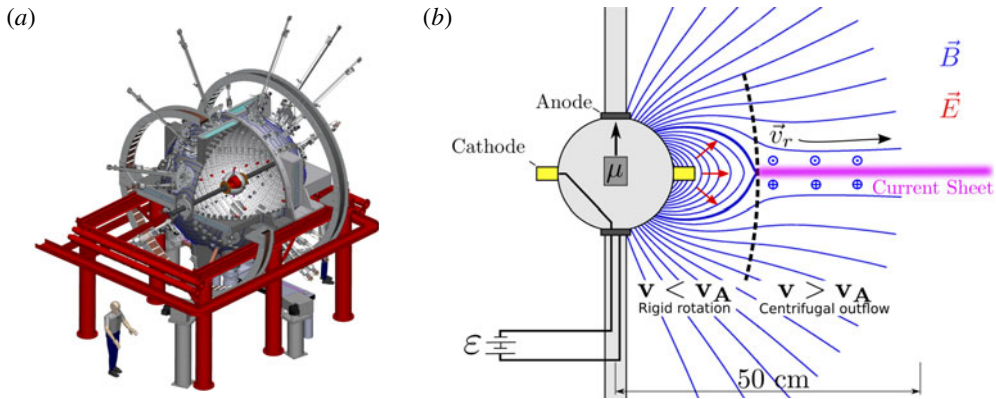


FIGURE 10. (a) WiPAL facility with centrifugal wind experiment installed and (b) proposed configuration showing the electromagnetic stirring scheme and Y-point.

closed magnetic topology breaks into an open configuration. This is expected to occur at the Alfvén radius, the location where the kinetic and magnetic energy densities are equal. WiPAL’s large volume, well-developed power supplies and comprehensive diagnostics make it suitable for experimental analysis of these active areas of research.

A laboratory analogue of a rotating, stellar magnetosphere is possible using the electrostatic stirring techniques developed for MPDX with the addition of a dipole magnetic field at the centre of the vessel. Through ECR heating, the dipole magnetosphere will be filled with confined plasma. Biased electrodes at the equatorial surface of the dipole will establish a cross-field potential gradient, leading to $\mathbf{E} \times \mathbf{B}$ stirring. As the plasma spins to critical velocity, a centrifugal wind will be launched. In this way, we can use a large cross-field potential to spin the magnetosphere and model the above astrophysical situations.

In preliminary experiments, an electrically insulated, spherical SmCo magnet ($r \simeq 10$ cm, surface field ~ 4 kG) will serve as the dipole source, shown in figure 10. ECR heating will produce plasma on the spherically symmetric 875 G surface. Using helium, expected temperatures and densities will be similar to prior MPDX experiments ($T_e \approx 5\text{--}20$ eV and $n_e \approx 10^{12}$ cm $^{-3}$). Equatorial cathodes, spaced ≈ 10 cm apart, will be biased up to 1 kV to establish a cross-field potential, producing axially aligned $\mathbf{E} \times \mathbf{B}$ rotation.

WiPAL’s existing diagnostics can be used for investigation of the Y-point and current sheet regions. The standard suite of Langmuir and Mach probes will be used for basic plasma measurements at the edge and will supplement the non-invasive measurements. A 2D, motor-controlled, 20 MHz resolution magnetic probe array will serve as the primary diagnostic. The magnetic probe will look for the characteristic Y-point opening of the magnetic field lines at the Alfvén radius and will explore the equatorial current sheet at larger radii.

Planned upgrades will explore other regimes. For example, obliquely rotating pulsars generate larger spin-down power than aligned rotators (Spitkovsky 2006) and provide a more realistic setting for studying current sheet reconnection. By supplementing the dipole magnet with phased coils, an obliquely rotating magnetosphere can be created. This will allow for experimental confirmation of the above prediction and characterization of the change in the undulating current sheets.

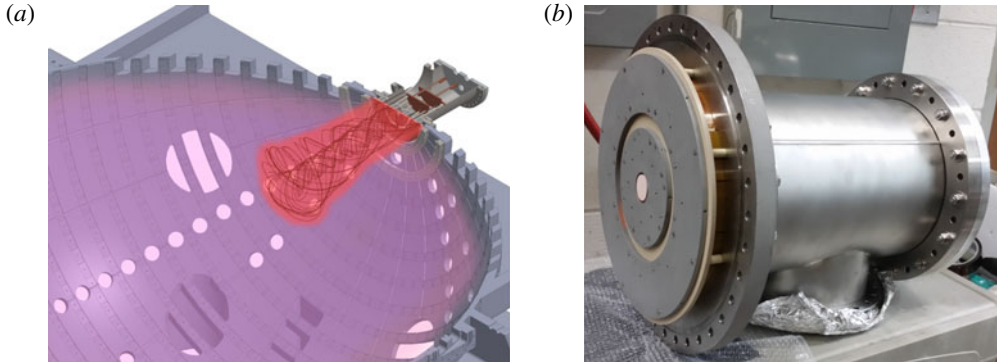


FIGURE 11. Experiment to study jet expansion into background, finite-pressure plasmas. Simulation of the jet is taken from Li *et al.* (2006) and superimposed onto the WiPAL plasma schematic, showing coaxial injection geometry. (b) The assembled pulsed jet source preparing for first tests.

3.6. Stability of astrophysical jets in background plasma

Astrophysical jets are collimated magnetized plasma outflows from accreting bodies such as active galactic nuclei, binary systems and young stellar objects. It is thought that jets could play a key role in angular momentum transport in accretion systems. Jets are launched and collimated in regions much smaller than the current resolution limits of observations, so the details of this process remain elusive. Certain models of the launching process predict that astrophysical jets arise due to magnetic fields in the accretion disk (Lovelace 1976; Blandford & Payne 1982; Spruit 2010). In these models, a dipole-like magnetic field is sheared by Keplerian rotation in the disk. This creates a large electric field between the centre and edge of the disk, driving current along the dipole field. Then $\mathbf{J} \times \mathbf{B}$ forces accelerate and collimate plasma, creating the jet structure. These jets should be susceptible to current-driven instabilities, but recently published theories suggest that the presence of external plasma pressure promotes collimation and enhances the stability of the jet structure out to large distances (Li *et al.* 2001, 2006; Lynden-Bell 2003).

The permanent magnet pulsed jet source (PM-PJS), shown in figure 11, creates an astrophysical jet-like plasma utilizing a design similar to that used by Hsu & Bellan (2002). A large voltage potential is created between two coplanar annuli (approximately 30 cm in diameter). This simulates the potential created via the aforementioned accretion disk shearing action. The background magnetic field in the astrophysical system is simulated using two antisymmetric rings of permanent magnets. The use of permanent magnets instead of electromagnets allows the source to maintain WiPAL's cusp-confining boundary condition. Neutral gas is injected via internal channels in both annuli, with ports placed at eight azimuthally symmetric pairs of magnetic field line foot points. This gas is ionized by the large voltage, creating eight filamentary loop structures. These loops merge and collimate, driving a magnetic jet into the centre of WiPAL.

This experiment complements Caltech experiments (Hsu & Bellan 2002, 2003; Moser & Bellan 2012) by studying the evolution of a magnetic jet evolving into a vacuum. Additionally, WiPAL allows the creation of a magnetic jet that propagates into a high- β background plasma. This will help clarify the relationship between jet stability and external plasma conditions (Li *et al.* 2001, 2006; Lynden-Bell 2003).

Future work will focus on the shock and precursors that are formed between the magnetized jet and the unmagnetized background plasma as predicted in Li *et al.* (2006) and on how the development of the kink instability could depend on the strength of the background pressure. Experimentally it will be possible to vary the target plasma pressure by more than two orders of magnitude. The properties of the expanding magnetic plume (speed, density, magnetic field) as well as the shock precursors will be measured using scanning probes similar to those used in the reconnection and centrifugal wind experiments.

3.7. Helicity injection and decaying turbulence

The generation of large-scale magnetic fields is a fundamental feature of many astrophysical systems. This dynamo action (as described in §3.2) is often attributed to a turbulent upscale transfer of small-scale magnetic helicity, $H = \int \mathbf{A} \cdot \mathbf{B} dV$. The upscale transfer process is ideally described as a local, self-similar inverse cascade where helicity is conserved and transferred to larger scales (Frisch *et al.* 1975; Ji 1999; Blackman & Ji 2006). In real systems, however, the transfer process is much more complex and can involve non-local transfer directly from the small to large scales as described in the turbulent alpha effect. The upscale spectral transfer of magnetic helicity has been explored extensively via direct numerical simulations (e.g. Alexakis, Mininni & Pouquet 2006). Understanding this upscale transfer of magnetic helicity is key to explaining the creation of the large-scale magnetic fields observed throughout the Universe.

In addition to upscale spectral transfer of helicity, transport in space is necessary for large-scale dynamo action. Large-scale dynamos can be sustained in systems with boundary conditions allowing the outflow of helicity. Roughly speaking, ejection of one sign of magnetic helicity allows helicity of the opposite sign to grow without violating helicity conservation. This idea was originally suggested on theoretical grounds by Blackman & Field (2001) and Vishniac & Cho (2001). Later, it was shown that magnetic eruptions associated with solar activity transmit a net helicity flux, suggesting that the solar dynamo meets these boundary conditions (Kusano 2002; Rust 2002; Liu *et al.* 2014; Pevtsov *et al.* 2014). In addition to the solar dynamo, this boundary condition effect is thought to occur in galactic dynamos driven by supernovae (Rafikov & Kulsrud 2000). There is evidence from numerical simulations that the generation of large-scale fields is promoted by boundary conditions that permit escape of magnetic helicity (Brandenburg & Sandin 2004; Käpylä, Korpi & Brandenburg 2010; Hubbard & Brandenburg 2012). Yet none of these ideas have been tested in the laboratory.

In the plasma physics community, helicity injection is primarily explored as a startup mechanism for magnetically dominated tokamak plasmas (Raman *et al.* 2003, 2010; Battaglia *et al.* 2009). Some laboratory astrophysical experiments that inject net helicity into plasma systems have also focused on magnetic reconnection and other instabilities that occur during Taylor relaxation of low- β plasmas (Jarboe 2005; Cothran *et al.* 2009; Gray *et al.* 2010). All of these experiments rely on helicity injection at large scales (comparable to the scale of the plasma volume) relaxing via magnetic instability to minimum-energy, helicity-conserving Taylor states in low- β plasmas (Taylor 1986). As a complement to these studies, we will inject helicity at small scales and use the large size of the WiPAL vessel to directly observe the upscale spectral transfer and transport of helicity in a high- β , dynamo-relevant plasma conditions.

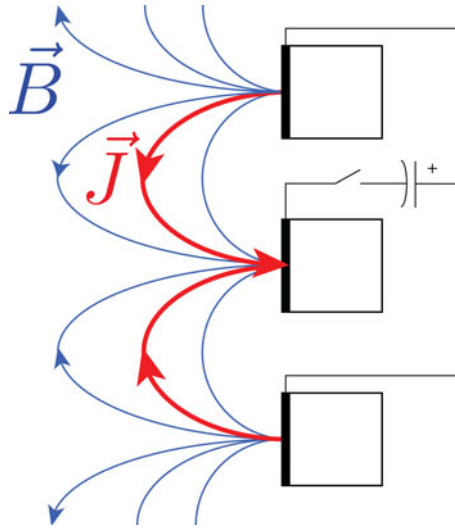


FIGURE 12. The axisymmetric ring cusp lends itself to a novel helicity injection experiment where currents, flowing between the magnetic pole faces, can be configured to inject small-scale magnetic helicity.

Generalizing the PM-PJS experiment discussed above (§3.6), helicity can be injected using the edge-localized cusp field inside WiPAL. A large potential can be applied between alternating rings, which will drive a current along cusp field lines and lead to an injection of helicity into the system without a guide field present (figure 12). By using all of the rings of permanent magnets inside the vessel, this helicity will be injected at a small ($\ell = 18$, $m = 0$) scale relative to the size of the vessel. The resulting rings of flux will then be blown off the wall into the bulk unmagnetized plasma with kinetic and magnetic energies near equipartition. In order to drive an upscale transfer instead of simple resistive diffusion, we require the resistive decay time to be much longer than the Alfvén time of this system. Cast in dimensionless terms, this means that the Lundquist number, $S \equiv \tau_r/\tau_A$, must be large. Using the high-power capacitor banks created for TREX, magnetic fields of $B \simeq 100$ G can be induced from current driven along the cusp field lines. For WiPAL discharge parameters, this corresponds to $S \simeq 1000$. Under these conditions, we expect helicity to undergo a turbulent transfer before resistive diffusion can dissipate the injected magnetic energy. Observing the transfer and transport of helicity in this set-up will complement dynamo studies conducted by MPDX and provide the astrophysics community with a laboratory environment to probe this fundamental process.

4. Conclusion

The Wisconsin Plasma Astrophysics Laboratory (WiPAL) provides the plasma astrophysics and fundamental plasma physics communities with a unique opportunity to study plasma phenomena in a laboratory setting. Hot, dense, unmagnetized and fully ionized plasmas are routinely created and confined in quiescent states for seconds as astrophysics experiments are performed. This user facility has been designed and operated with the goal of maximizing both plasma performance and flexibility of use.

To date, WiPAL has confined steady-state plasmas which are hotter and denser than any other large-scale non-magnetically dominated plasma device. These parameters have proven to be sufficient for both studying dynamo relevant regimes (MPDX) and providing high-Lundquist-number target plasmas for reconnection studies (TRES). In the longer term, the heating power will more than double as the cathode system is completed and the ECR system is installed.

Diagnosing the high-performance unmagnetized plasmas in WiPAL has been an area of intense focus. Arrays of robotically controlled magnetic and electrostatic probes are capable of mapping out large areas of WiPAL plasmas. Advanced optical diagnostics have been developed with the goal of reducing the additional loss area added by this suite of *in situ* probes. Millimetre-wave technology is used to power a compact heterodyne interferometer system for measuring electron density with high resolution. A Fabry–Perot interferometer is used to extract the ion velocity distribution. Finally, a complement of low-cost spectrometers coupled with collaborative modelling makes reliable estimates of the electron temperature and ionization fraction. All of these diagnostics provide a valuable set of data for every WiPAL discharge regardless of experiment.

Perhaps most significantly, the WiPAL facility has already demonstrated the ability to quickly change experimental configurations. This paper has outlined two major experiments already running on WiPAL (MPDX and TRES) as well as several new experiments in various stages of planning and implementation. We envision WiPAL transitioning in the near future to a user facility model in which investigators from outside the collaboration groups listed above could apply for and receive support to carry out experiments with technical support from the WiPAL staff.

Acknowledgement

The construction of the facility was supported by a National Science Foundation (NSF) Major Research Instrumentation grant. The MPDX and TRES research is now supported by NSF and the US Department of Energy (DoE) and the NSF Center for Magnetic Self Organization in Laboratory and Astrophysical Plasmas (CMSO). The helioseismology studies are part of a collaboration with NCAR (M.M.) and are supported by a NASA graduate fellowship (E.P.). The stellar wind experiment is a collaboration with Princeton University (A.S.) and is supported by an NSF graduate fellowship (D.E.).

REFERENCES

- ALEXAKIS, A., MININNI, P. D. & POUQUET, A. 2006 On the inverse cascade of magnetic helicity. *Astrophys. J.* **640** (1), 335.
- BARNES, S. A. 2007 Ages for illustrative field stars using gyrochronology: viability, limitations, and errors. *Astrophys. J.* **669**, 1167–1189.
- BATTAGLIA, D. J., BONGARD, M. W., FONCK, R. J., REDD, A. J. & SONTAG, A. C. 2009 Tokamak startup using point-source dc helicity injection. *Phys. Rev. Lett.* **102** (22), 225003.
- BLACKMAN, E. G. & FIELD, G. B. 2001 How astrophysical mean field dynamos can circumvent existing quenching constraints. *Phys. Plasmas* **8** (5), 2407–2414.
- BLACKMAN, E. G. & JI, H. 2006 Laboratory plasma dynamos, astrophysical dynamos and magnetic helicity evolution. *Mon. Not. R. Astron. Soc.* **369** (4), 1837–1848.
- BLANDFORD, R. D. & PAYNE, D. G. 1982 Hydromagnetic flows from accretion discs and the production of radio jets. *Mon. Not. R. Astron. Soc.* **199**, 883–903.

- BOFFARD, J. B., JUNG, R. O., LIN, C. C. & WENDT, A. E. 2010 Optical emission measurements of electron energy distributions in low-pressure argon inductively coupled plasmas. *Plasma Sources Sci. Technol.* **19** (6), 065001.
- BRANDENBURG, A. & SANDIN, C. 2004 Catastrophic alpha quenching alleviated by helicity flux and shear. *Astron. Astrophys.* **427**, 13–21.
- CHRISTENSEN-DALSGAARD, J. 2002 Helioseismology. *Rev. Mod. Phys.* **74** (4), 1073.
- COAKLEY, M. M., ROESLER, F. L., REYNOLDS, R. J. & NOSSAL, S. 1996 Fabry–Perot CCD annular-summing spectroscopy: study and implementation for aeronomy applications. *Appl. Opt.* **35** (33), 6479–6493.
- COOPER, C. M., WALLACE, J., BROOKHART, M., CLARK, M., COLLINS, C., DING, W. X., FLANAGAN, K., KHALZOV, I., LI, Y., MILHON, J., NORBERG, M., NONN, P., WEISBERG, D., WHYTE, D. G., ZWEIBEL, E. & FOREST, C. B. 2014 The Madison Plasma Dynamo Experiment: a facility for studying laboratory plasma astrophysics. *Phys. Plasmas* **21**, 013505.
- COTHRAN, C. D., BROWN, M. R., GRAY, T., SCHAFFER, M. J. & MARKLIN, G. 2009 Observation of a helical self-organized state in a compact toroidal plasma. *Phys. Rev. Lett.* **103** (21), 215002.
- DAUGHTON, W. & ROYTERSHEYN, V. 2012 Emerging parameter space map of magnetic reconnection in collisional and kinetic regimes. *Space Sci. Rev.* **172** (1–4), 271–282.
- DENG, B. H., BROWER, D. L., DING, W. X., WYMAN, M. D., CHAPMAN, B. E. & SARFF, J. S. 2006 High-speed three-wave polarimeter–interferometer diagnostic for Madison symmetric torus. *Rev. Sci. Instrum.* **77** (10), 10F108.
- DENG, C., BROWER, D. L., DING, W. X., ALMAGRI, A. F., ANDERSON, D. T., ANDERSON, F. S. B., GERHARDT, S. P., PROBERT, P. & TALMADGE, J. N. 2003 First results from the multichannel interferometer system on HSX. *Rev. Sci. Instrum.* **74** (3), 1625–1628.
- UD DOULA, A., TOWNSEND, R. H. D. & OWOCKI, S. P. 2006 Centrifugal breakout of magnetically confined line-driven stellar winds. *Astrophys. J. Lett.* **640** (2), L191.
- EGEDAL, J., LE, A. & DAUGHTON, W. 2013 A review of pressure anisotropy caused by electron trapping in collisionless plasma, and its implications for magnetic reconnection. *Phys. Plasmas* **20** (2013), 061201.
- FRISCH, U., POUQUET, A., LÉORAT, J. & MAZURE, A. 1975 Possibility of an inverse cascade of magnetic helicity in magnetohydrodynamic turbulence. *J. Fluid Mech.* **68** (4), 769–778.
- GALLET, B., AUMAÎTRE, S., BOISSON, J., DAVIAUD, F., DUBRULLE, B., BONNEFOY, N., BOURGOIN, M., ODIER, P., PINTON, J.-F., PLIHON, N., VERHILLE, G., FAUVE, S. & PÉTRÉLIS, F. 2012 Experimental observation of spatially localized dynamo magnetic fields. *Phys. Rev. Lett.* **108** (14), 144501.
- GOUGH, D. O. & MCINTYRE, M. E. 1998 Inevitability of a magnetic field in the sun’s radiative interior. *Nature* **394**, 755–757.
- GRAY, T., LUKIN, V. S., BROWN, M. R. & COTHRAN, C. D. 2010 Three-dimensional reconnection and relaxation of merging spheromak plasmas. *Phys. Plasmas* **17** (10), 102106.
- HERSHKOWITZ, N., LEUNG, K. N. & ROMESSER, T. 1975 Plasma leakage through a low- β line cusp. *Phys. Rev. Lett.* **35**, 277.
- HSU, S. C. & BELLAN, P. M. 2002 A laboratory plasma experiment for studying magnetic dynamics of accretion discs and jets. *Mon. Not. R. Astron. Soc.* **334** (2), 257–261.
- HSU, S. C. & BELLAN, P. M. 2003 Experimental identification of the kink instability as a poloidal flux amplification mechanism for coaxial gun spheromak formation. *Phys. Rev. Lett.* **90** (21), 1–4.
- HUBBARD, A. & BRANDENBURG, A. 2012 Catastrophic quenching in $\alpha\Omega$ dynamos revisited. *Astrophys. J.* **748** (1), 51.
- HUBBLE, A. A., BARNAT, E. V., WEATHERFORD, B. R. & FOSTER, J. E. 2014 The electron spatial distribution and leak width in a magnetic cusp. *Plasma Sources Sci. Technol.* **23** (2), 22001–22006.
- HWANG, K. J., GOLDSTEIN, M. L., WENDEL, D. E., FAZAKERLEY, A. N. & GURGIOLO, C. 2013 Cluster observations near reconnection X lines in Earth’s magnetotail current sheet. *J. Geophys. Res.* **118** (February), 4199–4209.

- ISKAKOV, A. B., SCHEKOCIHIN, A. A., COWLEY, S. C., MCWILLIAMS, J. C. & PROCTOR, M. R. E. 2007 Numerical demonstration of fluctuation dynamo at low magnetic Prandtl numbers. *Phys. Rev. Lett.* **98** (2), 208501.
- JARBOE, T. R. 2005 The spheromak confinement device. *Phys. Plasmas* **12** (5), 058103.
- Ji, H. 1999 Turbulent dynamos and magnetic helicity. *Phys. Rev. Lett.* **83** (16), 3198.
- Ji, H. & DAUGHTON, W. 2011 Phase diagram for magnetic reconnection in heliophysical, astrophysical, and laboratory plasmas. *Phys. Plasmas* **18** (11), 111207.
- KÄPYLÄ, P. J., KORPI, M. J. & BRANDENBURG, A. 2010 Open and closed boundaries in large-scale convective dynamos. *Astron. Astrophys.* **518**, A22.
- KATZ, N., COLLINS, C., WALLACE, J., CLARK, M., WEISBERG, D., JARA-ALMONTE, J., REESE, I., WHAL, C. & FOREST, C. B. 2012 Magnetic bucket for rotating unmagnetized plasma. *Rev. Sci. Instrum.* **83**, 063502.
- KHALZOV, I. V., BROWN, B. P., COOPER, C. M., WEISBERG, D. B. & FOREST, C. B. 2012a Optimized boundary driven flows for dynamos in a sphere. *Phys. Plasmas* **19**, 112106.
- KHALZOV, I. V., BROWN, B. P., KAPLAN, E. J., KATZ, N., PAZ-SOLDAN, C., RAHBARNIA, K., SPENCE, E. J. & FOREST, C. B. 2012b Resistive and ferritic-wall plasma dynamos in a sphere. *Phys. Plasmas* **19** (10), 104501.
- KHALZOV, I. V., COOPER, C. M. & FOREST, C. B. 2013 Fast dynamos in spherical boundary-driven flows. *Phys. Rev. Lett.* **111** (12), 125001.
- KUSANO, K. 2002 Numerical study of three-dimensional magnetohydrodynamic instability in the solar coronal magnetic arcades. *Astrophys. J.* **571** (1), 532–539.
- LATHROP, D. P. & FOREST, C. B. 2011 Magnetic dynamos in the lab. *Phys. Today* **64** (7), 40–45.
- LE, A., EGEDAL, J., DAUGHTON, W., ROYTERSHTEYN, V., KARIMABADI, H. & FOREST, C. 2015 Transition in electron physics of magnetic reconnection in weakly collisional plasma. *J. Plasma Phys.* **81**, 305810108.
- LI, H., LAPENTA, G., FINN, J. M., LI, S. & COLGATE, S. A. 2006 Modeling the large scale structures of astrophysical jets in the magnetically dominated limit. *Astrophys. J.* **643** (1), 92–100.
- LI, H., LOVELACE, R. V. E., FINN, J. M. & COLGATE, S. A. 2001 Magnetic helix formation driven by Keplerian disk rotation in an external plasma pressure: the initial expansion stage. *Astrophys. J.* **561** (2), 915–923.
- LIU, Y., HOEKSEMA, J. T., BOBRA, M., HAYASHI, K., SCHUCK, P. W. & SUN, X. 2014 Magnetic helicity in emerging solar active regions. *Astrophys. J.* **785** (1), 13.
- LOVELACE, R. V. E. 1976 Dynamo model of double radio sources. *Nature* **262**, 649–652.
- LYNDEN-BELL, D. 2003 On why discs generate magnetic towers and collimate jets. *Mon. Not. R. Astron. Soc.* **341**, 1360–1372.
- MACGREGOR, K. B. & CHARBONNEAU, P. 1999 Angular momentum transport in magnetized stellar radiative zones. IV. Ferraro's theorem and the solar tachocline. *Astrophys. J.* **519**, 911–917.
- MALIK, S. M., SRIDHARAN, K., FETHERSTON, R. P., CHEN, A. & CONRAD, J. R. 1994 Overview of plasma source ion implantation research at University of Wisconsin–Madison. *J. Vac. Sci. Technol. B* **12** (2), 843–849.
- MATT, S. P., BRUN, A. S., BARAFFE, I., BOUVIER, J. & CHABRIER, G. 2015 The mass-dependence of angular momentum evolution in sun-like stars. *Astrophys. J. Lett.* **799**, L23 (6pp.).
- MESTEL, L. 1968 Magnetic braking by a stellar wind. *Mon. Not. R. Astron. Soc.* **138** (3), 359–391.
- MIESCH, M. S. & HINDMAN, B. W. 2011 Gyroscopic pumping in the solar near-surface shear layer. *Astrophys. J.* **743**, 79 (25pp.).
- MONCHAUX, R., BERHANU, M., AUMAÎTRE, S., CHIFFAUDEL, A., DAVIAUD, F., DUBRULLE, B., RAVELET, F., FAUVE, S., MORDANT, N., PÉTRÉLIS, F., BOURGOIN, M., ODIER, P., PINTON, J.-F., PLIHON, N. & VOLK, R. 2009 The Von Kármán sodium experiment: turbulent dynamical dynamos. *Phys. Fluids* **21** (3), 035108.
- MONCHAUX, R., BERHANU, M., BOURGOIN, M., MOULIN, M., ODIER, P., PINTON, J.-F., VOLK, R., FAUVE, S., MORDANT, N., PÉTRÉLIS, F., CHIFFAUDEL, A., DAVIAUD, F., DUBRULLE, B., GASQUET, C., MARIÉ, L. & RAVELET, F. 2007 Generation of a magnetic field by dynamo action in a turbulent flow of liquid sodium. *Phys. Rev. Lett.* **98** (4), 044502.

- MOSER, A. L. & BELLAN, P. M. 2012 Magnetic reconnection from a multiscale instability cascade. *Nature* **482** (7385), 379–381.
- PEVTSOV, A. A., BERGER, M. A., NINDOS, A., NORTON, A. A. & VAN DRIEL-GESZTELYI, L. 2014 Magnetic helicity, tilt, and twist. *Space Sci. Rev.* **186** (1), 285–324.
- PHILIPPOV, A. A. & SPITKOVSKY, A. 2014 Ab initio pulsar magnetosphere: three-dimensional particle-in-cell simulations of axisymmetric pulsars. *Astrophys. J. Lett.* **785** (2), L33.
- PRIEST, E. & FORBES, T. 2000 *Magnetic Reconnection*. Cambridge University Press.
- RAFIKOV, R. R. & KULSRUD, R. M. 2000 Magnetic flux expulsion in powerful superbubble explosions and the α - Ω dynamo. *Mon. Not. R. Astron. Soc.* **314** (4), 839–848.
- RAMAN, R., JARBOE, T. R., NELSON, B. A., IZZO, V. A., O'NEILL, R. G., REDD, A. J. & SMITH, R. J. 2003 Demonstration of plasma startup by coaxial helicity injection. *Phys. Rev. Lett.* **90** (7), 075005.
- RAMAN, R., MUELLER, D., NELSON, B. A., JARBOE, T. R., GERHARDT, S., KUGEL, H. W., LEBLANC, B., MAINGI, R., MENARD, J., ONO, M., PAUL, S., ROQUEMORE, L., SABBAGH, S., SOUKHANOVSKII, V. & NSTX RESEARCH TEAM 2010 Demonstration of tokamak ohmic flux saving by transient coaxial helicity injection in the national spherical torus experiment. *Phys. Rev. Lett.* **104** (9), 095003.
- RUST, D. M. 2002 Helicity build-up and the role of CMEs. In *American Astronomical Society Meeting Abstracts #200*, Bulletin of the American Astronomical Society, vol. 34, p. 751; <http://adsabs.harvard.edu/abs/2002AAS...200.6503R>.
- SCHEKOCHIHIN, A. A., COWLEY, S. C., TAYLOR, S. F., MARON, J. L. & MCWILLIAMS, J. C. 2004 Simulations of small-scale turbulent dynamo. *Astrophys. J.* **612**, 276.
- SCHMITZ, O., BEIGMAN, I. L., VAINSHTEIN, L. A., SCHWEER, B., KANTOR, M., POSPIESZCZYK, A., XU, Y., KRYCHOWIAK, M., LEHNEN, M., SAMM, U., UNTERBERG, B. & THE TEXTOR TEAM 2008 Status of electron temperature and density measurement with beam emission spectroscopy on thermal helium at textor. *Plasma Phys. Control. Fusion* **50** (11), 115004.
- SENGUPTA, A. 2009 Magnetic confinement in a ring-cusp ion thruster discharge plasma. *J. Appl. Phys.* **105** (9), 093303.
- SPENCE, E., REUTER, K. & FOREST, C. B. 2009 Numerical simulations of a spherical plasma dynamo experiment. *Astrophys. J.* **700**, 470–478.
- SPIEGEL, E. A. & ZAHN, J.-P. 1992 The solar tachocline. *Astron. Astrophys.* **265**, 106–114.
- SPITKOVSKY, A. 2006 Time-dependent force-free pulsar magnetospheres: axisymmetric and oblique rotators. *Astrophys. J. Lett.* **648** (1), L51.
- SPRUIT, H. C. 2010 Theory of magnetically powered jets. In *The Jet Paradigm* (ed. T. Belloni), pp. 233–263. Springer.
- STIRLING, W. L., RYAN, P. M., TSAI, C. C. & LEUNG, K. N. 1979 Magnetic multipole line-cusp plasma generator for neutral beam injectors. *Rev. Sci. Instrum.* **50** (1), 102–108.
- TAYLOR, J. B. 1986 Relaxation and magnetic reconnection in plasmas. *Rev. Mod. Phys.* **58** (3), 741.
- THOMPSON, M. J. 2014 Solar physics: surface waves and helioseismology. http://solarscience.msfc.nasa.gov/images/internal_rotation_mjt.jpg.
- THOMPSON, M. J., CHRISTENSEN-DALSGAARD, J., MIESCH, M. S. & TOOMRE, J. 2003 The internal rotation of the Sun. *Annu. Rev. Astron. Astrophys.* **41**, 599–643.
- TOWNSEND, R. H. D., RIVINIUS, T., ROWE, J. F., MOFFAT, A. F. J., MATTHEWS, J. M., BOHLENDER, D., NEINER, C., TELTING, J. H., GUENTHER, D. B., KALLINGER, T., KUSCHNIG, R., RUCINSKI, S. M., SASSELOV, D. & WEISS, W. W. 2013 MOST observations of Ori E: challenging the centrifugal breakout narrative. *Astrophys. J.* **769** (1), 33.
- VISHNIAC, E. T. & CHO, J. 2001 Magnetic helicity conservation and astrophysical dynamos. *Astrophys. J.* **550** (2), 752–760.
- WANG, S., WENDT, A. E., BOFFARD, J. B., LIN, C. C., RADOVANOV, S. & PERSING, H. 2013 Noninvasive, real-time measurements of plasma parameters via optical emission spectroscopy. *J. Vac. Sci. Technol. A* **31** (2), 021303.